Structural properties of ceramic powders of CeO_2:Eu_2O_3

M.R. González-García, A. García-Murillo, F.J. Carrillo-Romo, A.D. Alcantar-Mendoza, I.D. Cabrera-Rios

This work aimed to synthesize and characterize CeO_2:Eu_2O_3 ceramic powders with molar concentrations (Ce:Eu = 100:0, 98:2, 95:5, 92:8, 90:10, and 70:30). The gels were heat treated at 700 °C for 24 hours to induce crystallization of the ceramic powders. The materials were characterized by X-ray diffraction (XRD), X-ray photoelectron spectroscopy (XPS), spectroscopy infrared spectroscopy (IR), Raman spectroscopy, scanning electron microscopy (SEM), photoluminescence (PL), and cathodoluminescence (CL). The results reveal that all ceramic powders presented a cubic (fluorite) structure with modifications in the lattice parameters as the Eu^{3+} concentrations changed. Furthermore, the Eu_2O_3 diffraction pattern allowed the complete identification of the crystal planes. The crystallite sizes were 64, 22, 30, 38, 40, and 50 nm for the Ce:Eu^{3+} ceramic powders at 100:0, 98:2, 95:5, 92:8, 90:10, and 70:30, respectively. XPS results showed a Ce^{3+}/Ce^{4+} ratio of 0.27%. The IR spectrograms show the M-O bands attributable to CeO_2 at 460, 560, 860, and 1200 cm^{-1}. The results of the Raman spectra show three main bands at 260, 468, and 600 cm^{-1}, which are associated with the F_{2g} vibration mode of octahedral local symmetry found around the CeO_2 lattice and the defect-induced mode related to the presence of oxygen vacancies due to the existence of Ce^{4+} ions. The particles exhibited morphological changes due to the change from the doped phase to the solid solution. The higher the concentration of Eu^{3+}, the greater its agglomeration and size. The ceramic powders showed luminescent properties exhibiting emissions mainly by the $^5D_0$-$^7D_2$ transition of Eu^{3+} and the 30 mol% sample showed higher luminescent intensity in cathodoluminescence.

Introduction

Luminescent ceramic nanomaterials are indispensable due to their properties and potential applications in gas sensors, fuel cells, polishing materials, phosphors, energy storage materials, catalysts, and biosensors [1]. The nanomaterials applied in these areas are usually composed of systems doped with elements that modify their properties to benefit them; the most used are the lanthanides. This group of elements ranges from lanthanum (La-57) to lutetium (Lu-71) and is used in all kinds of new technologies due to their unique chemical and physical properties. Additionally, they exhibit photoluminescent properties as phosphor material, which result from f-f electron transitions in their partially filled f orbitals [2-4]. A semiconductor that has been widely studied due to its high chemical stability, high UV radiation absorption, good dielectric strength, high vacancy oxygen due to the facile interconversion between Ce^{4+} and Ce^{3+}, and high refractive index is cerium oxide (CeO_2) [4-6].

Cerium oxide comprises a Ce^{4+} cation coordinated with 8 O^{2-} anions forming a CeO_2 (cubic structure, fluorite-type) with a special Fm-3m group [7]. Furthermore, it possesses excellent properties as a host material due to the absence of electrons in the 4f layer since it can be partially replaced to form a solid solution and improve the luminescence response [8]. Cerium oxide can be doped with lanthanide ions, especially europium (Eu-63), because the transitions $^5D_0$-^7F_j cause an intense red-orange emission. Transition $^7F_2$ is hypersensitive [9] and can be excited by different types of energy. In addition, effective energy conversion and transfer processes can be generated, improving the luminescent response. Another important aspect is the solubility of the doping ion in the host material lattice. In this sense, the Eu^{3+} ion is an excellent candidate because the ionic radius of Eu^{3+} (0.1066 nm) is like Ce^{3+} (0.1143 nm) and Ce^{4+} (0.097 nm); for this reason, it promotes the inclusion of the ion effectively [10]. In 2021, D'Achille *et al.* synthesized CeO_2 nanomaterials doped with Eu^{3+} at different molar concentrations [11]. They obtained a fluorite-type cubic crystalline structure without secondary phases, indicating the formation of a CeO_2:Eu^{3+} solid solution. They reported the relationship between morphology and fluorescent properties, namely, that surface chemistry and crystal defects impacted Eu^{3+} emissions.

Other authors, such as Secu *et al.*, used the sol-gel method to obtain silica microspheres embedded with Eu^{3+}-doped cerium oxide nanocrystals [12]. The results showed that Ce^{4+} ions were successfully replaced by Eu^{3+} ions. The structural, optical, mechanical, and other properties revealed that these luminescent materials based on the system CeO_2:Eu^{3+} are attractive potential candidates for photonics and multifunctional biomarkers applications. Ankita *et al.* also studied cerium oxide nanoparticles doped with Eu^{3+} at different molar concentrations (2, 4, 6, 8%) [13]. Structural, chemical, compositional, and magnetic analysis revealed the development of materials that can be applied in sustainable wastewater treatment and spintronics. The results revealed that at these concentrations, there is no structural change, only changes in the lattice parameters and a shift in peak position (2θ) towards lower angles; also, the presence of reticular defects was observed due to the increase in the concentration of Eu indicating substitution of Eu^{3+} in CeO_2 lattice.

It should be noted that different types of synthesis, chemical and physical, have been reported for obtaining

M. del R. González-García ✉, A. García-Murillo ✉,
F. J. Carrillo-Romo, A. D. Alcantar-Mendoza,
I. D. Cabrera-Rios
Particle technology, Instituto Politécnico Nacional, Centro de Investigación e Innovación Tecnológica, Azcapotzalco, Cd. Mx., 02250, México.

Presented at the Luminescence phenomena *Simposium, XVII Intl. Conf. on Surfaces, Materials, and Vacuum, SMCTSM,* September 23rd to 27th, 2024. Ensenada, BC, Mexico.
Received: September 25th, 2024.
Accepted: May 24th, 2025.
Published: June 30th, 2025.

https://doi.org/10.47566/2025_syv38_1-250601

nanomaterials of lanthanide elements, such as hydrothermal, solid-state, microwave, and co-precipitation methods; however, the sol-gel method is an incredibly effective way of synthesizing of nanomaterials based on solid solutions. It allows controlling variables such as gelation time, temperature, and solvents [9]. Furthermore, it is possible to obtain nanomaterials with excellent properties from different rare earth oxides with acids to form different metallic salts, such as nitrates, sulfates, and chlorides. For example, Carrillo *et al.* reported results obtained from Yb_2O_3 using a sol-gel method driven by epoxide and citric acid to reduce gelation time and possibly obtain ceramic powders after heat treatment [14]. The precursors used were ytterbium and europium oxides with hydrochloric acid to form the metal salt, and subsequently, with supercritical drying, they obtained the aerogel. In addition, they studied structural, morphological, and luminescent properties.

This research aimed to study the behavior of the structural, chemical, morphological, and luminescent properties of CeO_2:Eu_2O_3 ceramic powders by incorporating the Eu^{3+} ion at different molar concentrations (Ce:Eu^{3+} = 100:0, 98:2, 95:5, 92:8, 90:10, and 70:30). These materials could contribute to research on nanomaterials, with applications in the biological, ceramic, and optoelectronic fields.

Experimental details

The synthesis of CeO_2:Eu_2O_3 ceramic powders at different molar concentrations (CeO_2:Eu_2O_3 = 100:0, 98:2, 95:5, 92:8, 90:10, and 70:30) was realized by the sol-gel method. All the precursors used were Sigma-Aldrich brand: cerium oxide (CeO_2), europium oxide (Eu_2O_3), hydrochloric acid (HCl), propylene oxide (PO, CH_3CHCH_2O), citric acid monohydrate ($C_6H_8O_7{\cdot}H_2O$), and absolute ethyl alcohol (EtOH, CH_3CH_2OH). A solution containing 0.1 g of CeO_2 with the corresponding concentration of Eu^{3+} was prepared with 1 ml of HCl diluted in distilled water (1:5).

The mixture was kept constant, stirring at 80 °C for 90 minutes to dissolve the precursors completely. Subsequently, 2 ml of EtOH and PO were added to promote hydrolysis and condensation reactions. A total of 2.1 ml of the chelating agent ($C_6H_8O_7{\cdot}H_2O$) was added at room temperature to cause the formation of the gel through aging. Finally, heat treatment was performed at 700 °C for 24 hours to promote the formation of crystalline structures. The CeO_2:Eu_2O_3 ceramic powders synthesized at CeO_2:Eu_2O_3 = 100:0, 98:2, 95:5, 92:8, 90:10, 70:30, and 0:100, were labeled Ce, Ce:Eu2, Ce:Eu5, Ce:Eu8, Ce:Eu10, Ce:Eu30, and Eu_2O_3 respectively.

Characterizations techniques

The structural, chemical, morphological, elemental, and photoluminescence properties of the ceramic powders obtained by the sol-gel method were analyzed with the following characterization techniques. X-ray diffraction (XDR) with a Bruker Eco D8 ADVANCE diffractometer was used to determine the crystalline structure of CeO_2 and the behavior of Bragg reflections when introducing the Eu^{3+} ions. The XRD pattern of the powder was recorded using CuKα1 radiation (1.5418 Å) with a fraction angle range of 15° to 80° (0.02 steps). The lattice parameters were analyzed by Rietveld refinement performed in HighScore. X-ray photoelectron spectroscopy was performed with Thermo Scientific K-ALPHA Surfaces Analysis to analyze the ceramic powders to investigate the local atomic environment of the surface of materials. Infrared spectroscopy (IR) using KBr pellets was performed with a Perkin Elmer Spectrum 65 Spectrometer to analyze the ceramic powders and identify the characteristic vibrational absorption bands of CeO_2 with Eu^{3+} ions. They were analyzed in a range from 2000 to 400 cm^{-1}. The morphological characteristics of the samples were examined with a JSM 6701F—670 scanning electron microscope (SEM). Also, the average particle size was calculated using IMAGEJ software. The average was determined with a Gauss bell curve to see the particle size distribution. The information was complemented by a quantitative elemental analysis with energy dispersive spectroscopy (EDS) at resolutions of 10,000x using an INCAx-act detector from Oxford Instruments. Finally, the samples were analyzed by photoluminescence (PL) in a Hitachi F-7000 fluorometer with a 150 W xenon lamp and by cathodoluminescence (CL) applying a voltage of 6 kV with a current of 0.3 mA.

Results and discussion

Structural analysis: X-ray diffraction

The ceramic powders were characterized by X-ray diffraction (XRD); the diffractograms are shown in Figure 1. All the diffractograms show (111), (200), (220), (311), (222), (400), (331), and (420) crystalline planes, which, according to ICSD chart 98-015-5604, are attributed to a cubic structure (fluorite) with a Fm-3m space group [15-18].

The patterns revealed the inclusion of the Eu^{3+} ions since no structural changes or additional peaks were observed. According to Xu *et al*., this behavior indicates that the Eu^{3+} cations partially replaced the Ce ions to form a solid solution [19], which means that the dopant ions in this case were wholly dissolved in the solid ceria solution, as reported by Anirban *et al*. [4].

The *a*/*b*/*c* parameters of undoped cerium registered values of 5.407 Å were very similar to those reported by Soni *et al*. [20]. Furthermore, as the concentration of the dopant ion

Table 1. Structural values of the CeO_2:Eu_2O_3 ceramic powders.

CeO_2:Eu_2O_3			
Samples	**Lattice parameters** (Å)		**Crystallite size** (nm)
	a/*b*/*c*	GOF	
Ce	5.407	0.75	64
Ce:Eu2	5.413	0.73	22
Ce:Eu5	5.420	0.47	30
Ce:Eu8	5.425	0.80	38
Ce:Eu10	5.430	0.79	40
Ce:Eu30	5.433	0.55	50

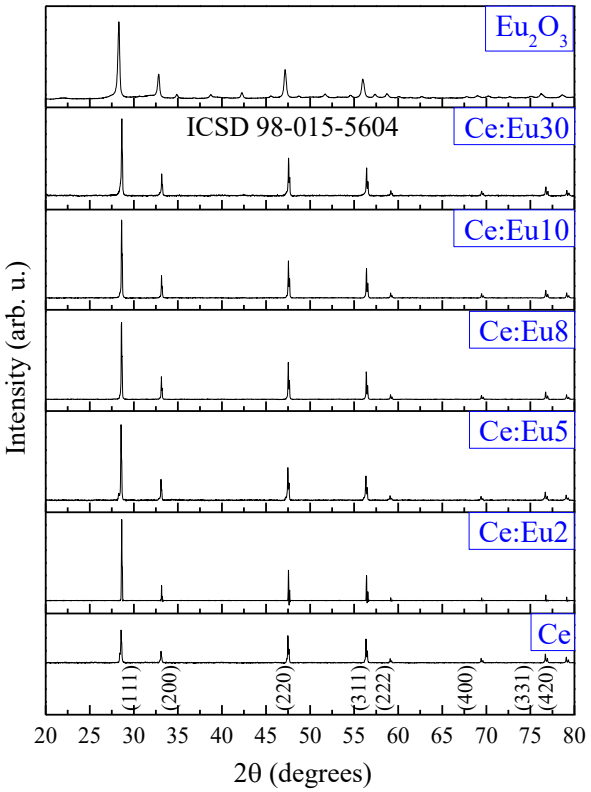

Figure 1. Diffractograms of the CeO_2:Eu_2O_3 ceramic powders at different concentrations with heat treated at 700 °C for 24 hours.

(Eu^{3+}) increased, the values of *a* (*b* and *c*) increased, which is related to the ionic radius of the dopant ion.

Eu^{3+} and Ce^{4+} ions collectively created oxygen vacancies in the CeO_2 lattice to maintain charge equilibrium, which has also been reported for further lattice expansion. These variations in lattice parameters indicate the effect of the doping concentrations of Eu^{3+} ions on the CeO_2 [21,22].

Figure 2 shows the behavior of the lattice parameters with respect to concentration. It is indicated that with increasing Eu^{3+} concentration, a slight deviation of the parameters occurred since the ionic radius of Eu^{3+} (0.1066 nm) is more significant than that of Ce^{4+} (0.097 nm). Judging by this, a partial substitution of Eu^{3+} ions by Ce^{4+} ions and their inclusion in the structure was achieved [23]. According to the literature, high concentrations of doping ions (Eu^{3+}) could promote phase mixing. This behavior can be observed in Figure 2 by the appearance of phase transitions. However, according to the obtained diffractograms, adding Eu^{3+} concentration at low concentrations does not modify the structure; no additional peaks confirm the formation of a solid solution.

The crystallite sizes were 64, 22, 30, 38, 40, and 50 nm for the CeO_2:Eu_2O_3 ceramic powders at concentrations of 100:0, 98:2, 95:5, 92:8, 90:10, and 70:30, respectively [21,23]. Increasing the concentration Eu^{3+} causes an increase in the lattice parameter. This is due to the stiffness generated by the increased lattice stress caused by substituting Eu^{3+} for Ce^{4+} ions. Adding the dopant ion (Eu^{3+}) in the structure of the host (CeO_2) promotes modifications in the size of the crystallite. The crystallite size of the host matrix is 64 nm, it decreases

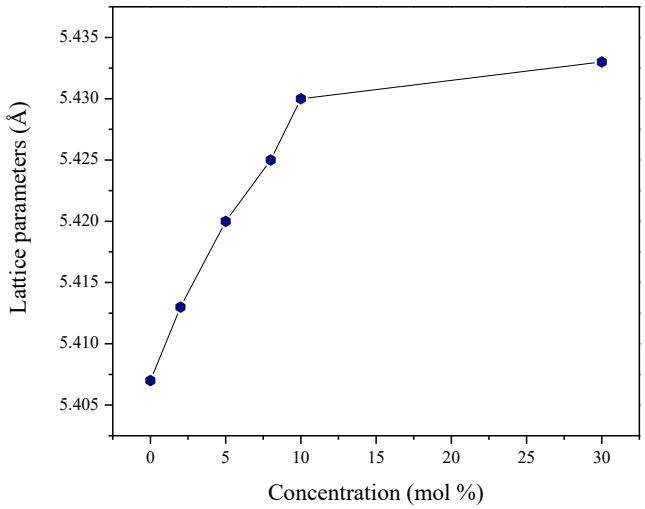

Figure 2. Relationship of the lattice parameters with respect to the Eu^{3+} concentration.

when doped with 2 mol% Eu^{3+} ions; and then it begins to increase due to the formation of new crystallites as the Eu^{3+} concentration rises, until it reaches the 30 mol% solid solution phases, where a size closer to the matrix is reached [24].

Figure 3 shows the behavior of the crystallite size as the concentration of Eu^{3+} increases. It can be observed that the addition of Eu^{3+} promotes different phase transitions and the growth of new crystals due to the high concentrations of Eu^{3+} (30 mol%). At this concentration, doping is no longer considered, but rather a mixture of phases. In addition, the crystallite size is very important because it is related to asymmetry, modifying the positions of the inversion centers in the crystal lattice. In this way, a change in the intensity of the luminescence of ceramic powders can be promoted [25].

The degree of crystallinity of all the synthesized samples was determined using the following expression:

$$\text{Cristallinity} = \frac{\text{Area of cristallinity peaks (Cristalline+amorphous)}}{\text{Area of all peaks}} 100 \qquad (1)$$

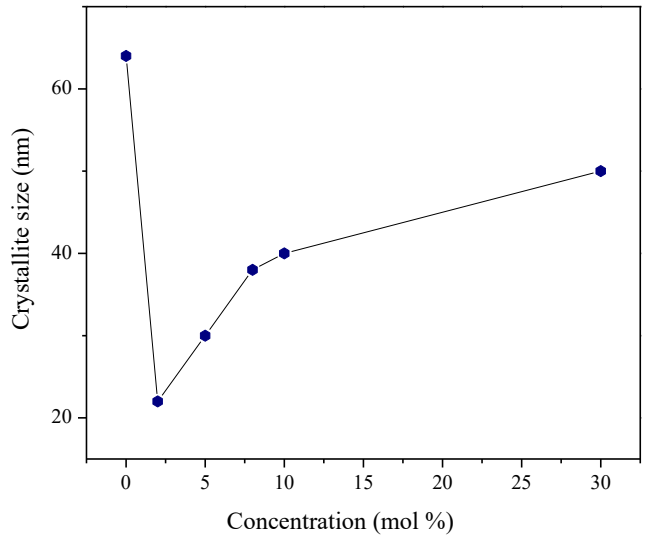

Figure 3. Relationship of the crystallite size with respect to the Eu^{3+} concentration.

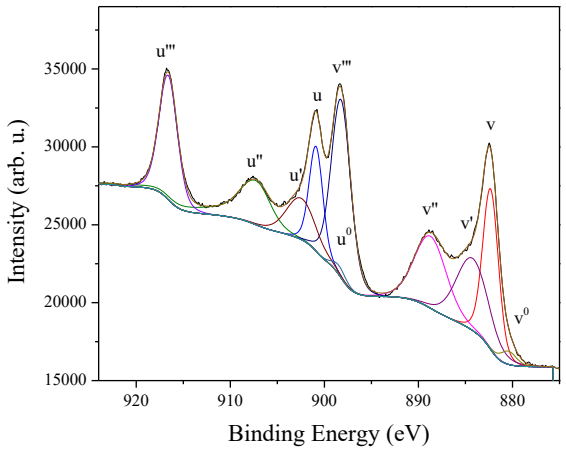

Figure 4. Ce3d XPS spectra of the CeO_2 ceramic powders.

The obtained values were 64, 50, 48, 56, 65, and 76% for ceramic powders at 100:0, 98:2, 95:5, 92:8, 90:10 and 70:30, respectively. In this sense, it is concluded that the sample Ce:Eu30 stands out due to its structural properties.

X-ray photoelectron spectroscopy (XPS)

Pure CeO_2 ceramic powders were characterized by XPS and are shown in Figure 4. The results revealed signals on the surface of the material, which are attributed to Ce, oxygen 1s (522-539eV), and carbon 1s (280-294) [26]. The atomic content of carbon is present due to the environment. In this sense, the ratio of Ce^{3+} and Ce^{4+} was 21.29% and 78.72% hence the result was 0.27%. Multiplets attributed to the central holes of the spin-orbit splitting were observed as in Ce^{4+} $3d_{5/2}$ and $3d_{3/2}$ at approximately 916.6 and 888.72 eV (v/u, v''/u'' and v'''/u'''), respectively [27]. In XPS spectroscopy, different physical processes can be observed during photoemission, such as shake-up, shake-down, energy loss, and plasmons; these are peaks commonly known as satellites. In this sense, the u''' peak refers to a satellite of Ce^{4+} located at high binding energies [28]. In addition, Ce^{3+} at 902.48 and 884.24 eV are attributed to the final states assigned to $3d_{3/2}$ and $3d_{5/2}$ (v^0/u^0 and v'/u'), respectively [29]. Table 2. reports the values obtained for the relative content of the concentrations of the electronic states Ce^{3+} and Ce^{4+} present on the material's surface (5-7 nm).

Table 2. XPS values of Ce^{4+}/Ce^{3+}.

Ce^{4+}		Ce^{3+}	
Binding Energy (eV)	Atomic%	Binding Energy (eV)	Atomic%
882.33	11.95	884.24	10.94
900.89	10.24	902.48	8.48
888.72	10.96	880.41	0.98
907.31	12.36	898.43	0.89
898.23	16.6		
916.6	16.61		
Total %	78.72	Total %	21.29

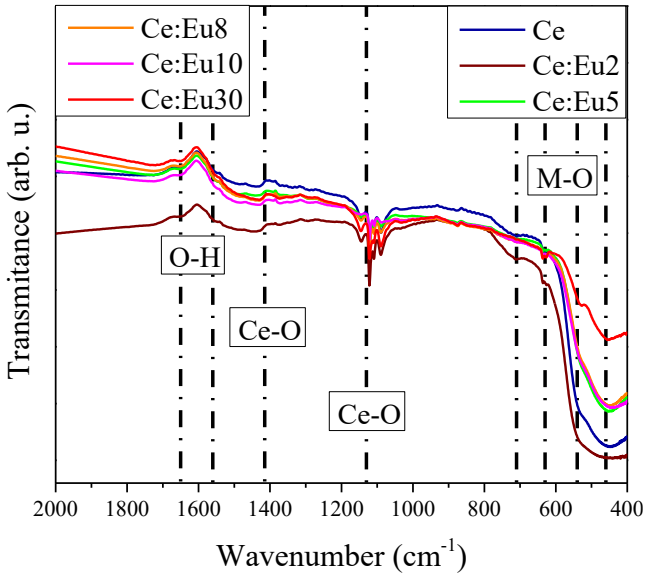

Figure 5. IR spectrograms of the CeO_2:Eu_2O_3 ceramic powders at different concentrations, heat treated at 700 °C for 24 hours.

Infrared (IR) and Raman spectroscopy

The transmittance spectrum was reported in Figure 5. The identified bands were at 540 and 460 cm^{-1} for M-O interaction, indicating the formation of CeO_2, as seen in Hernandez *et al*., Utara *et al*., and Gnanam *et al*. [30-32]. Approximately 1670 cm^{-1}, O-H bonds are attributed to water molecules usually absorbed on the surface. During the manipulation of the samples to characterize them, they are commonly exposed to the environment; for this reason, O-H can be observed [33]. The vibration peaks of the C-O chemical bonds near 1415 cm^{-1} correspond to the remaining compounds [34]. Previous work has reported the behavior of the band positions. Figure 5 shows the spectra of pure CeO_2 and Eu^{3+} doped ceramic powders at different concentrations. It is observed that as the concentration of Eu^{3+} in the matrix increases, the M-O positions shift the wavelength to a lower position; this behavior is because Eu^{3+} ions are lighter than Ce^{4+} ions, indicating the presence of Eu^{3+} ions in the matrix structure (CeO_2) [35].

Raman spectroscopy is commonly used to study the vibrational behavior of material lattices to detect structural differences in oxide compounds. It is also very useful because it makes it possible to study the effects of concentrations of small quantities of doping ions on the symmetry of nanocrystalline structures and their defects [36]. CeO_2:Eu_2O_3 ceramic powders at different concentrations were characterized by Raman spectroscopy and the results were reported in Figure 6 in an interval of 300-800 cm^{-1} they reveal a peak of greater intensity at approximately 468 cm^{-1}, which can be attributed to the fluorite F_{2g} vibration mode of octahedral local symmetry found around the CeO_2 network, which corresponds to the type of crystalline structure in agreement with X-ray diffraction results. This vibration has also been reported by Mi *et al*, Feng *et al*., Su *et al*., and Wang *et al*. [37-40]. Furthermore, a low-intensity disallowed band was found at 600 cm^{-1} outside the ideal lattice of the cubic fluorite-type

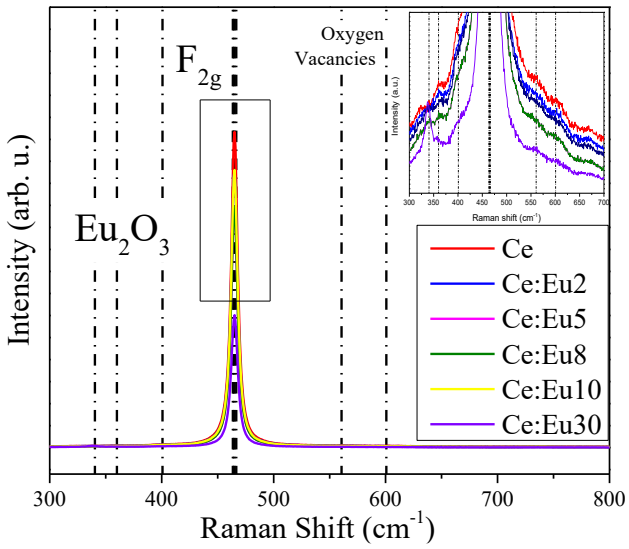

Figure 6. Raman spectra of the CeO_2:Eu_2O_3 ceramic powders at different concentrations with heat treated at 700 °C for 24 hours.

structure of CeO_2. The disallowed modes do not contribute to the Raman spectra and arise due to the lattice defects [13]. When the Eu^{3+} concentration was increased, a shift to lower wavenumbers was generated; i.e., 468 cm^{-1}, 463 cm^{-1}, 464 cm^{-1}, 465 cm^{-1} for the pure CeO_2 samples and those doped with Eu^{3+} at 2, 8, 10, 30 mol%, respectively. This process could be explained by the appearance of deformations and defects in the lattice, which reduce the energy of the Ce–O vibrations or by the substitution of Eu^{3+}/Ce^{4+} ions [13].

The presence of the phonon mode was observed, which is a characteristic of the cubic phase of Eu_2O_3, characterized by bands about 340, 360, and 400 cm^{-1} in low intensities. Therefore, there is displacement of the peak position due to the increase in the concentration of Eu^{3+}. The presence of the characteristic bands of oxygen defects in the CeO_2 structure and the absence of the phonon band Eu_2O_3 reinforce that Eu^{3+} cations are replacing Ce^{4+} cations on the CeO_2 lattice. According to Kumar *et al*. rare earth sesquioxides exhibit different vibrational modes at low and high Raman shift (Fg, Ag, Eg, Eg+Fg…) [41]. The most intense active mode is located at approximately 339 cm^{-1}. In this sense, these data agree with the results obtained and it can be concluded that Eu^{3+} is present in the CeO_2 matrix.

A small band at 600 cm^{-1} can be observed in the pure CeO_2 sample [42]. This band can be related to the difference in crystallite size and the presence of Ce^{4+} cations on the surface of the solid that promotes a non-stoichiometric condition [43]. The band's appearance at 560 cm^{-1} is attributed to intrinsic oxygen vacancies (Frenkel-type oxygen vacancies) due to Ce^{4+}ions. Frenkel-type oxygen vacancies begin to form on the surface of the subsoil and progress to form a CeO_2 mass [44].

The most predominant peak was identified at 468 cm^{-1} and was observed to be more intense in the pure matrix (CeO_2). As the Eu^{3+} concentration increased, the intensity decreased. This is because fewer oxygen vacancy defects were formed, as reported by Wang *et al*. [45].

According to Anirban *et al*., Cerrato *et al*., and Min *et al*., the distribution of oxygen vacancies in doped cerium oxide nanomaterials is strongly related to the ionic radius of dopant cations [4,46,47]. This means that the size difference between the dopant cations and the matrix may play a vital role in defect clustering.

Morphological analysis: Scanning electron microscopy

Micrographs of the CeO_2 (100:0) (Figure 7a), CeO_2:Eu8 (92:8) (Figure 7b), CeO_2:Eu10 (90:10) (Figure 7c), and CeO_2:Eu30 (70:30) (Figure 7d) ceramic powders were shown in Figure 4; they were taken at 10,000x magnifications to analyze the behavior of morphology with the concentration of the Eu^{3+}.

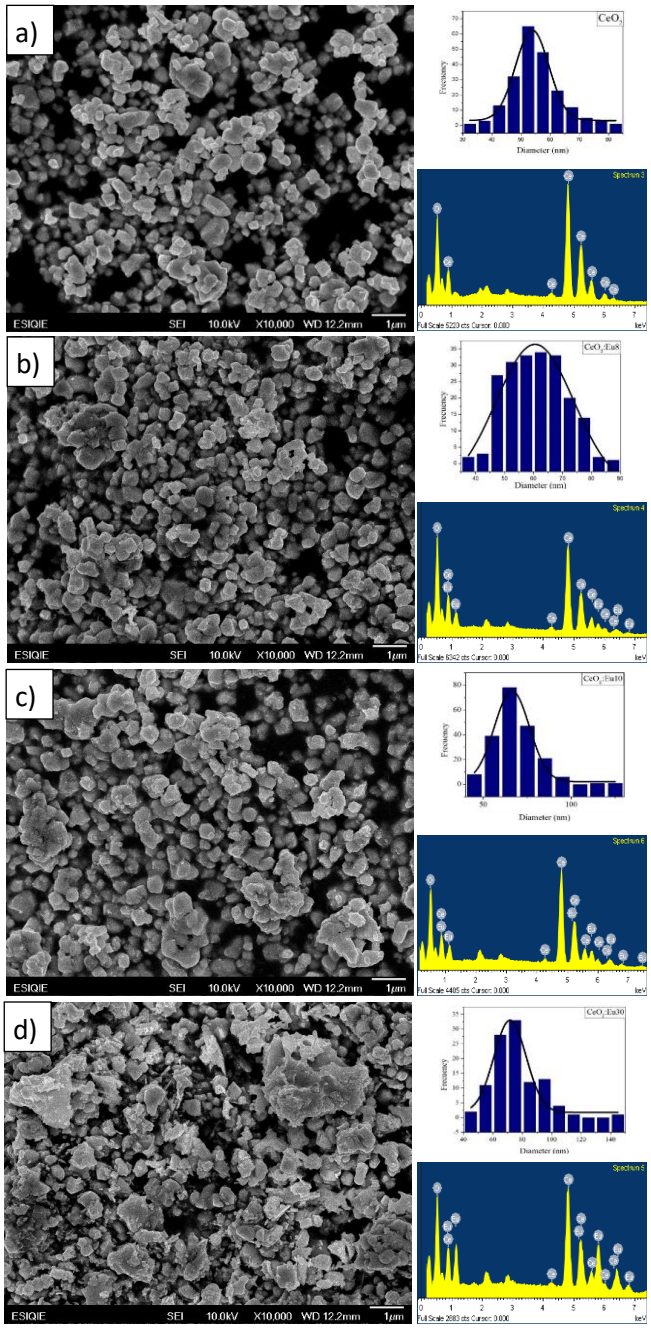

Figure 7. Micrographs of the CeO_2:Eu_2O_3 ceramic powders at (a) 100:0, (b) 98:2, (c) 90:10, and (d) 70:30, heat treated at 700 °C for 24 hours.

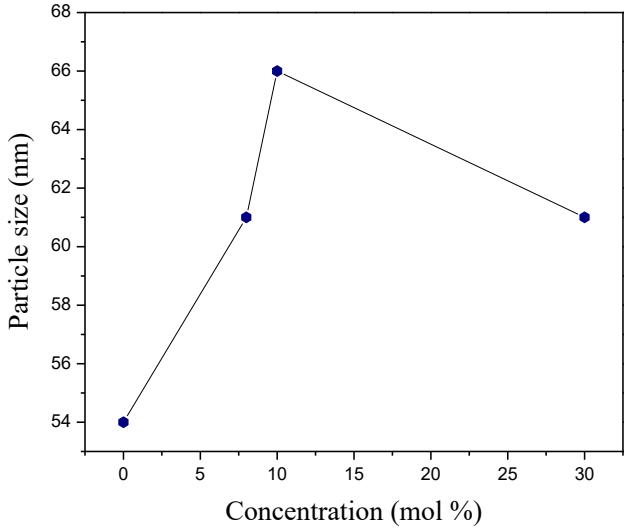

Figure 8. Relationship of the particle size with respect to the Eu^{3+} concentration.

In micrographs (a), (b), and (c), some cubic morphologies were observed. The particles exhibit dispersion and a low degree of agglomeration compared to the Ce:Eu30 particles; as the concentration of Eu^{3+} increased, the morphologies became non-uniform and irregular. Particles of different sizes are observed at a concentration of 30 mol% Eu^{3+}. Besides, according to Mangour [48] they do not have a specific morphology; they are only considered round, elongated, and irregular particles. Furthermore, at 30 mol% the agglomeration increases, and they are less dispersed. [49].

The average particle size was calculated using IMAGEJ software. The sizes were 54, 61, 66, and 61 nm for the CeO_2 (100:0), CeO_2:Eu8 (92:8), CeO_2:Eu10 (90:10), and CeO_2:Eu30 (70:30). Particle growth resulted from including Eu^{3+} ions in the CeO_2 structure, as shown in Figure 8. In this regard, the selection of the concentration is essential. In samples 7 (b-d), very similar sizes were reported when the europium ion concentration was incorporated because the radius of the Eu^{3+} ion is very similar to that of Ce^{4+}, which promotes a slight increase in size.

The results obtained from the dispersive X-ray spectroscopy (EDS) were obtained. The weight percentage of each sample is in good agreement with the concentration used for Eu^{3+} doping; namely, the weight percentages of CeO_2 (100:0), CeO_2:Eu8 (92:8), CeO_2:Eu10 (90:10), and CeO_2:Eu30 (70:30) were 9.62, 13.48, and 29.37 wt%, respectively. It is important to consider several factors that could cause weight loss in the samples. For example, handling the gels and the heat-treated ceramic powders during synthesis could reduce the final precursor weight in the samples.

Luminescence analysis:

a) Photoluminescence

The excitation and emission spectra of all the CeO_2:Eu_2O_3 ceramic powders are shown in Figure 9. Excitation spectra of the charge transfer band (CBT) by the interaction between O^{2-} and Eu^{3+} were observed around 270 nm. A band at

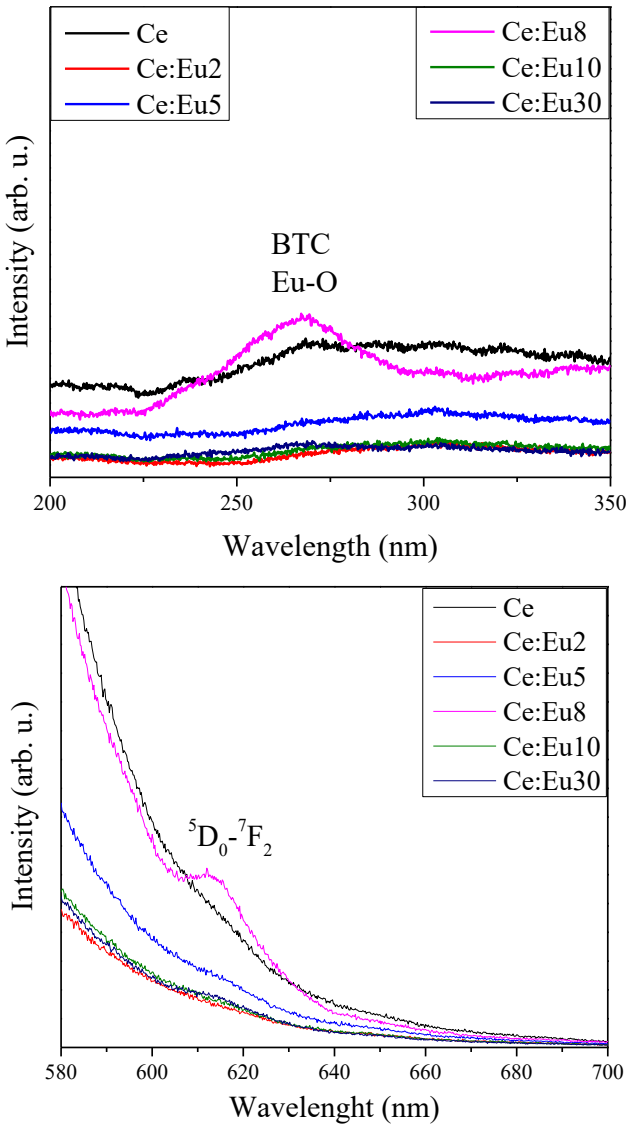

Figure 9. Photoluminescence and excitation spectra of the CeO_2:Eu_2O_3 ceramic powders at different concentrations with heat treated at 700 °C for 24 h.

612 nm attributed to the $^5D_0 \rightarrow {}^7F_2$ d transition was observed in the emission spectra. This transition was generated due to the electronic dipolar transition, as reported in [50-53].

The dominant energy transition was $^5D_0 \rightarrow {}^7F_2$, which is known to be a hypersensitive transition that is generated at sites without inversion symmetry. Another energy transition assignable to the Eu^{3+} ion was not located. An essential condition for materials to emit photoluminescence is the degree of crystallinity. In this respect, the diffractograms obtained from the structural analysis show that the sample Ce:Eu8 had the most defined peaks compared to the other samples. All the spectra showed the $^5D_0 \rightarrow {}^7F_2$ transition at low intensities because the Eu^{3+} ion concentration used was too high and promoted the luminescence quenching. On the other hand, possibly CeO_2 absorbed all the energy because the Eu^{3+} ions did not promote high amounts of oxygen vacancies but instead were positioned in interstitial sites and did not generate the europium energy transfer band with

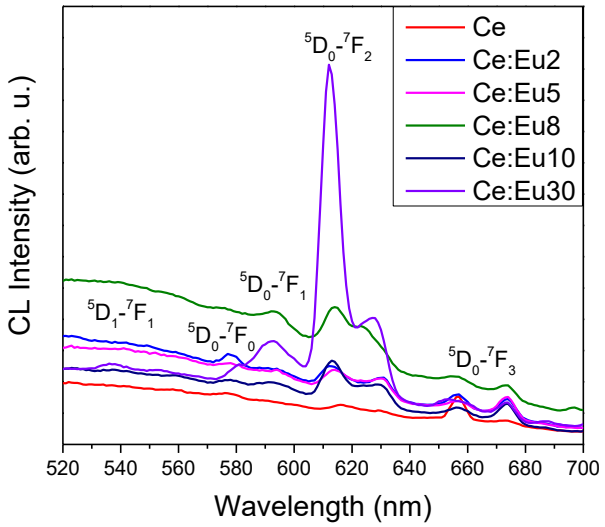

Figure 10. Cathodoluminescence spectra of the CeO_2:Eu_2O_3 ceramic powders at different concentrations with heat treated at 700 °C for 24 hours.

oxygen. Due to the ionic radius of Ce^{4+} is very similar to the ionic radius of Eu^{3+}, a direct substitution occurs. The ionic radius is very different in the case of Ce^{4+} with Eu^{3+}. Therefore, interstitial incorporation occurs, but it induces significant stress in the lattice. For this reason, interstitial incorporation could occur but charge compensation is required, for example, with oxygen vacancies [48-54].

Properly selecting the doping ion concentration is necessary because it is directly related to the emission response of the synthesized ceramic powders. In this sense, according to the results obtained in Figure 6, two phenomena occur as follows: a) There is emission from ceramic powders at lower concentrations (8 mol%), because there is a more significant number of excited Eu^{3+}, b) cross-relaxation occurs when the concentration is higher (30 mol%) of Eu^{3+}, and the emission intensity decreases drastically. This behavior has been reported by García *et al*. [35].

b) Cathodoluminescence

Europium-doped cerium oxide ceramic powders were characterized by cathodoluminescence. The obtained spectra are reported in Figure 10. The characteristic energy transitions of Eu^{3+} were observed. $^5D_0$-$^7F_1$, $^5D_0$-$^7F_2$, and $^5D_0$-$^7F_3$ at 592, 612, and approximately 658-675 nm, respectively. The most predominant band was at 612 nm due to the hypersensitive $^5D_0 \rightarrow {}^7F_2$ transition in the CeO_2 lattice, suggesting no low symmetry inversion core [55].

The 30% sample was the one that presented the highest cathodoluminescence emission because the energy used in CL is more potent compared to the energy used in photoluminescence. In this sense, it allows the observation of other transitions that are not usually detected in photoluminescence, such as the $^5D_1 \rightarrow {}^7F_1$ transition. According to the results obtained in cathodoluminescence, the higher the concentration, the greater the emission intensity [56]. Furthermore, the luminescent emission is directly related to the crystalline materials due to the asymmetry and the position of the inversion centers. In this sense, the degree of crystallinity obtained in XRD of the CeO_2 sample doped with 30 mol% Eu^{3+} promotes a more significant cathodoluminescent emission.

Conclusions

The results obtained confirm that the sol-gel method is an effective technique for the synthesis of CeO_2 ceramic powders doped with Eu^{3+} at various concentrations. Physicochemical and structural characterizations reveal that the incorporation of Eu^{3+} induces significant modifications in properties such as particle size (54, 61, 66, and 61 nm), crystallite size (64, 22, 30, 38, 40, 50 nm), and lattice parameters (5.407, 5.413, 5.420, 5.425, 5.430, 5.433 Å), likely associated with phase transitions. It was observed that the sample with the highest dopant concentration (Ce:Eu30) exhibited notable structural, morphological, and compositional changes, as well as a self-quenching effect in luminescence, although it showed the highest intensity in cathodoluminescence studies due to the hypersensitive transition ($^5D_0 \rightarrow {}^7F_2$) at 612 nm generated by the electronic dipolar transition. These findings highlight the importance of optimizing the dopant concentration to enhance the material's properties without compromising its stability. Finally, it is suggested that future research focus on strategies to enhance the luminescent response of the material, given its potential in medical, ceramic, and optoelectronic applications.

Acknowledgements

The authors thank CONAHCYT for financial support through a postgraduate scholarship for González-García, Alcantar-Mendoza, and Cabrera-Rios. Thanks to SIP-IPN for projects 20241486 and 20241489; to the CREA laboratory, CNMN, ESIQIE, and CICATA Legaria for the characterization of the materials obtained; to the Sociedad Mexicana de Ciencia y Tecnología de Superficies y Materiales A.C. for a student grant awarded to González-García to attend the XVIIICSMV. The authors also would like to thank Henry Jankiewicz for the editing work that he did for this paper and M. García Murillo for her assistance.

References

[1]. A. Singhania, *Ind. Eng. Chem. Res.* **56**, 28 (2017).
[2]. A. Rangaswamy, P. Sudarsanam, B.M. Reddy, *J. Rare Earths* **33**, 1162 (2015).
[3]. S. Gnanam, J. Gajendiran, J.R. Ramya, K. Ramachandran, S. Gokul Raj, *Chem. Phys. Lett.* **763**, 138217 (2021).
[4]. Sk. Anirbana, A. Duttaa, *Solid State Ion.* **309**, 137 (2017).
[5]. T. El-Achari, F. Goumrhar, L.B. Drissi, R.A. Laamara, *Phys. B: Condens. Matter* **601**, 412443 (2021).
[6]. C. Chesneau, J. Poostforooshan, B. Chevalier, A.M, Arias, V. Olszok, A. Hinzpeter, A.P. Weber, S. Belbekhouche, *Surf. Interfaces* **51**, 104682 (2024).
[7]. S. Li, X. Lu, S. Shi, L. Chen, Z. Wang, Y. Zhao, *Front. Chem.* **8**, 348 (2020).
[8]. T. Zhang, W. Wang, F. Gu, W. Xu, J. Zhang, Z. Li, T. Zhu, G. Xu, Z. Zhong, F. Su, *Appl. Cat. B: Environ.* **312**, 121385 (2022).
[9]. T. Senden, A. Meijerink, *J. Lumin.* **177**, 254 (2016).
[10]. L. Lin, X. Ma, S. Li, M. Wouters, V. Hessel, *Front. Chem.*

Sci. Eng. **13**, 501 (2019).
[11]. A.E. D'Achille, R.M. Wallace, J.L. Coffer, *Nanoscale Adv.* **12**, 1212 (2021).
[12]. C. Secu, C. Bartha, E. Matei, C. Radu, M. Secu, *Magnetochemistry* **8**, 22 (2022).
[13]. A. Ankita, S. Chahal, S. Singh, S. Kumar, P. Kumar, *Environ. Sci. Pollut. Res.* **31**, 1276 (2024).
[14]. F. Carrillo-Romo, A. Alcantar-Mendoza1, A. García-Murillo, M. Díaz-Cruz, *J. Aust. Ceram. Soc.* **59**, 763 (2023).
[15]. W. Zhao, J. Rong, W. Luo, L. Long, X. Yao, *Appl. Surf. Sci.* **579**, 152176 (2022).
[16]. T. Ema, P. Gyu-Choi, S. Takami, Y. Masuda, *ACS Appl. Mater. Interfaces* **14**, 56998 (2022).
[17]. S. Gao, W. Zhang, H. Zhou, D. Chen, *J. Rare Earths* **36**, 986 (2018).
[18]. A.A. Fakhrabadi, R. Saravanan, M. Jamshidijam, R.V. Mangalaraja, M.A. Gracia, *J. Saudi Chem. Soc.* **19**, 505 (2015).
[19]. Y. Xu, L. Gao, Z. Ding, *Materials* **15**, 8971 (2022).
[20]. S. Soni, S. Kumar, B. Dalela, S. Kumar, P.A. Alvi, S. Dalela, *J. Alloys Compd.* **752**, 520 (2018).
[21]. R. Saravanan, M.J. Jam, R.V. Mangalaraja, M.A. Gracia, *J. Saudi Chem. Soc.* 9, 505 (2015).
[22]. Z. Yang, Z. Yin, Z. Zhao, J. Yu, J. Li, Z. Ren, G. Yu, *Mater. Chem. Phys.* **240**, 122148 (2020).
[23]. T. Ema, P.C Gyu, S. Takami, Y. Masuda, *ACS Appl. Mater Interfaces* **14**, 56998 (2022).
[24]. Y. Zhang, N. Ding, T. Zheng, S. Jiang, B. Han, J. Lv, *J. Non-Cryst. Solids* **441**, 74 (2016).
[25]. D. Ríos, A.G. Murillo, F.J.C. Romo, *Ceram. Int.* **49**, 11230 (2023).
[26]. M.E. Khan, M.M. Khan, M.H. Cho, *Nature* **7**, 5928 (2017).
[27]. E. Bêche, P. Charvin, D. Perarnau, S. Abanades, G. Flamant, *Surf. Interface Anal.* **40**, 264 (2008).
[28]. L. Wang, L. Zhuang, H. Xin, Y. Huang, D. Wang, *Open J. Inorg. Chem.* **5**, 12 (2015).
[29]. O.S. Bezrkovnyia, M. Vorokhtab, M. Małeckaa, W. Mistaa, L. Kepinskia, *Catal. Commun.* **135**, 105875 (2020).
[30]. Y. Hernández-Castillo, M. García-Hernández, A. López-Marure, J.H. Luna-Domínguez, P.Y. López-Camacho, A.J. Morales-Ramírez, *Ceram. Int.* **45**, 2303 (2019).
[31]. S. Utara, S. Hunpratub, S. Pinitsoontorn, S. Phokha, *Results Phys.* **30**, 104890 (2021).
[32]. S. Gnanam, V. Rajendran, *J. Alloys Compd.* **735**, 1854 (2018).
[33]. S.A. Abid, A.A. Taha, R.A. Ismail, M.H. Mohsin, *Environ. Sci. Pollut. Res.* **27**, 30479, (2020).
[34]. Y. Chen, N. Huang, Y. Liang, *Ionics* **27**, 4347 (2021).
[35]. V.M. García Ramírez, A. García Murillo, F. de J. Carrillo Romo, A. Cervantes Tobón, N. Cayetano Castro, *Bull. Mater. Sci.* **46**, 75 (2023).
[36]. W. Zhao, J. Rong, W. Luo, L. Long, X. Yao, *Appl. Surf. Sci.* **579**, 152176 (2022).
[37]. R. Mi, D. Li, Z. Hu, R.T. Yang, *ACS Catal.* **11**, 7876 (2021).
[38]. Z. Feng, Q. Ren, R. Peng, S. Mo, M. Zhang, M. Fu, L. Chen, D. Ye, *Catal. Today* **332**, 177 (2019).
[39]. Z. Su, W. Yang, C. Wang, S. Xiong, X. Cao, Y. Peng, W. Si, Y. Weng, M. Xue, J. Li, *Environ. Sci. Technol.* **54**, 12684 (2020).
[40]. P. Wang, J. Wang, J. Shi, X. Du, X. Hao, B. Tang, A. Abudula, G. Guan, *Mol. Catal.* **492**, 111027 (2020).
[41]. S. Kumar, R. Prakash, V.K. Singh, *Rev. Adv. Sci. Eng.* **4,** 247 (2015).
[42]. N.S. Leel, M. Kiran, P.A. Alvi, B. Dalela, S. Kumar, S. Dalela, *Ceram. Int.* **50**, 8448 (2024).
[43]. A.A.G. Santiago, N.F.A. Neto, E. Longo, C.A. Paskocimas, F.V. Motta, M.R.D. Bomio, *J. Mater. Sci. Mater. Electron.* **30**, 11508 (2019).
[44]. J. Ahire, B.M. Bhanage, *Catal. Lett.* **152**, 3284 (2022).
[45]. M. Wang, N. Shang, W. Gao, X. Cheng, S. Gao, C. Wang, *Fuel* **354**, 129433 (2023).
[46]. E. Cerrato, E. Gaggero, P. Calza, M.C. Paganini, *Chem. Eng. J. Adv.* **10**, 100268 (2022).
[47]. P. Min, S. Zhang, Y. Xu, R. Li, *Appl. Surf. Sci.* **448**, 435 (2018).
[48]. B. AL-Mangour, Powder metallurgy of stainlesssteel: state-of-the art, challenges, and developments. In: *Stainless Steel: Microstructure, Mechanical Properties and Methods of Application*, Ed. A.K. Basak (Nova Science Publishers, 2015) p. 37-80.
[49]. M.L. Camacho-Ríos, R. A. Ochoa-Gamboa, W. Antunez, D. Lardizabal, *Microsc. Microanal.* **25**, 1792 (2019).
[50]. S. Milad, A. Nsar, Z. Hassan, K.Y. Cheong, W.F. Lim, W.F. Lim, *J. Mater. Sci. Mater. Electron.* **34**, 810 (2022).
[51]. L. Li, H.K. Yang, B.K. Moon, Z. Fu, C. Guo, J.H. Jeong, S.S. Yi, K. Jang, H.S. Lee, *J. Phys. Chem.* **113**, 610 (2009).
[52]. C. Li, Q. Xiao, Y. Fu, Y. Liang, C. Liu, Y. Zhuang, L. Xia, *J. Non-Cryst. Solids* **552**, 120453 (2021).
[53]. L. He, Y. Su, J. Lanhong, S. Shi, *J. Rare Earths* **33**, 791 (2015).
[54]. L.D. Sonawane, A.S. Mandawade, L.N. Bhoye, H.I. Ahemad, S.S. Tayade, Y.B. Aher, A.B. Gite, Latesh K. Nikam, S.D. Shinde, G.H. Jain, G.E. Patil, M.S. Shinde, *Inorg. Chem. Commun.* **164**, 112313 (2024).
[55]. I. Camps, A. Mariscal, L.C. Barrio, R. Serna, *Phys. Status Solidi A* **215**, 1800260 (2018).
[56]. H. Wu, C.B. Poitras, M. Lipson, M.G. Spencer, *Appl. Phys. Lett.* **88**, 011921 (2006).

The results included in this article were presented at the *Luminescence phenomena Simposium, of the XVII International Conference on Surfaces, Materials, and Vacuum, SMCTSM*, September 23rd to 27th, 2024. Ensenada, BC, Mexico. (see Editorial Note https://doi.org/10.47566/2024_syv37_0-240001).